ARTICLE

Strain-Induced Bandgap Enhancement of InSe Ultrathin Films with Self-Formed Two-Dimensional Electron Gas

Zhimo Zhang, Yuan Yuan, Weiqing Zhou, Chen Chen, Shengjun Yuan, Hualing Zeng, Ying-Shuang Fu,* and Wenhao Zhang*

Read Online

ACCESS | Metrics & More | Article Recommendations | SI Supporting Information

ABSTRACT: Atomically thin indium selenide (InSe) is a representative two-dimensional (2D) family that have recently attracted extensive interest for their intriguing emerging physics and potential optoelectronic applications with high-performance. Here, by utilizing molecular beam epitaxy and scanning tunneling microscopy, we report a controlled synthesis of InSe thin films down to the monolayer limit and characterization of their electronic properties at atomic scale. Highly versatile growth conditions are developed to fabricate well crystalline InSe films, with a reversible and controllable phase transformation between InSe and In_2Se_3. The band gap size of InSe films, as enhanced by quantum confinement, increases with decreasing film thickness. Near various categories of lattice imperfections, the band gap becomes significantly enlarged, resulting in a type-I band alignments for lateral heterojunctions. Such band gap enhancement, as unveiled from our first-principles calculations, is ascribed to the local compressive strain imposed by the lattice imperfections. Moreover, InSe films host highly conductive 2D electron gas, manifesting prominent quasiparticle scattering signatures. The 2D electron gas is self-formed via substrate doping of electrons, which shift the Fermi level above the confinement-quantized conduction band. Our study identifies InSe ultrathin film as an appealing system for both fundamental research and potential applications in nanoelectrics and optoelectronics.

KEYWORDS: InSe films, strain effect, band bending, two-dimensional electron gas, molecular beam epitaxy growth, scanning tunneling microscopy, density functional theory calculations
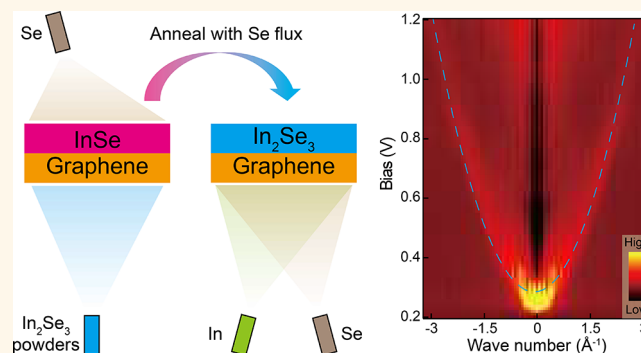
The inspiring discovery of graphene has triggered a wide range of upsurge in 2D van der Waals (vdW) materials for decades,[1] which consist of a layered structure with covalently bonded intralayer and weakly vdW interacted interlayer. Enthusiasm has been ignited not only by their exotic emerging physics with diverse dimensionalities,[2−5] but also by their promising potentials in the areas of next-generation optoelectronic and photovoltaic devices.[6−8] Among the tremendous studied candidates, indium selenide represents a rapid-growing family with progressive attentions endowing intriguing mechanical, electronic and optical properties.[9] Particularly, layered indium selenide belongs to a large family of complex compounds with various stoichiometries, involving InSe, In_2Se_3, In_3Se_4, In_4Se_3, In_6Se_7, etc. Even for the same stoichiometry, distinct phases and crystal structures may stably coexist.[10] As such polytropic stoichiometries and multivariate alignments of atomic configurations within a vdW layer, the fabrication of indium selenide films with high quality is still

challenging by mixed phases and poor crystallinity, especially in the epitaxial growth process.[10−14]

As a prototypical material, bulk InSe comprises covalently bonded tetralayer (TL) in a Se−In−In-Se sequence, as shown in Figure 1a,b. It belongs to a typical III−V semiconductor that can be stablized down to the 2D limit, thus becomes widely exploited with exotic properties. Few-layer InSe exhibits some superior prospects over the transition metal chalcogenides or black phosphorus,[1,8,9] such as strong photoresponsivity, fast response time,[15] luminescent excitons with anisotropic
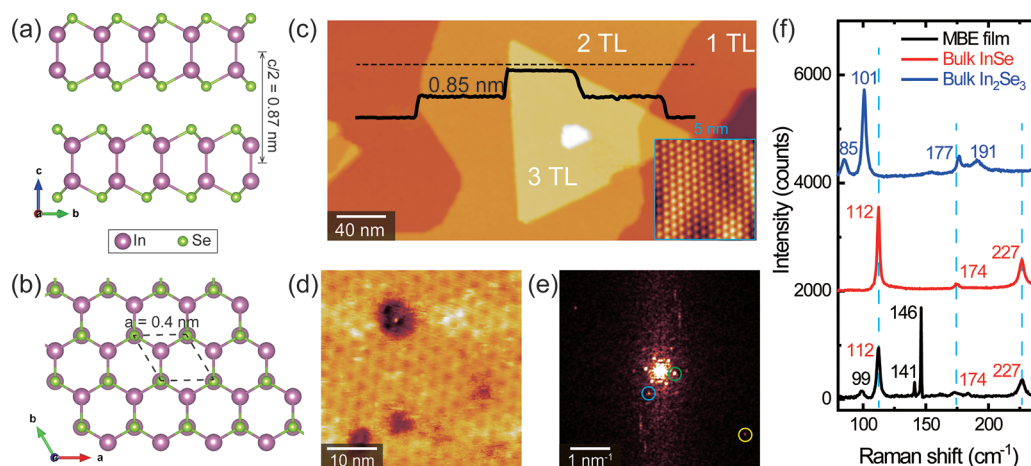
Figure 1. Structure and STM morphologies of layered InSe films. (a), (b) Crystal structures in the side and top view for a TL InSe film, respectively. The black dashed rhombus shows the unit cell. (c) STM morphology of InSe ultrathin films. A height profile along the dashed black line is labeled with a height of 0.85 nm for each single TL step (scanning size: 350×170 nm^2, bias voltage V_{bias} = +2.0 V, tunneling current I_t = 10 pA). Inset shows the atomically resolved image of Se atoms (5×5 nm^2, V_{bias} = +100 mV, I_t = 100 pA). (d) The zoom-in STM image of InSe surface (40×40 nm^2, V_{bias} = +300 mV, I_t = 50 pA). (e) 2D FFT of (d). Three types of diffraction spots are highlighted by yellow, cyan and green circles, corresponding to the 1×1 Se-terminated lattice, SiC-6×6 reconstruction and a 3.2 nm Moiré period, respectively. (f) Representative Raman spectra of bulk InSe and In$_2$Se$_3$ samples, associated with the MBE-grown thin films. The black, red, and blue numbers of Raman shifts indicate the signals from the SiC substrate, InSe, and In$_2$Se$_3$ films, respectively.

characters[16,17] and tunable current-induced spin polarization by spin−orbital coupling effect.[18,19] Besides, by engineering InSe with other 2D vdW materials, it is highly compelling to build type-II heterostructures with radiative optical transitions irrespective of lattice mismatches.[20] Furthermore, 2D electron gas (2DEG) can be induced in InSe flakes ($\geq$6 TL) with considerably high electron mobility exceeding 10^3 cm^2·V^{-1}·s^{-1} at room temperature, enabling the observations of anomalous optical response and quantum Hall effect.[21,22] All these outstanding properties point out that InSe is beneficial for room-temperature field-effect transistors with conceivable applications in optoelectronic and spintronic devices.

However, the above-mentioned excellent properties of InSe were studied in few layers so far. Constructing miniaturized nanoelectronics devices ideally requires the study of its electronic properties down to the monolayer limit. Moreover, the interface with the ultrathin InSe films provides an appealing protocol for engineering its physical properties. By virtue of its superplastic deformability,[23] the interface may pose strain to the InSe ultrathin films, which are predicted to modulate its band gap and the free-carrier mobility.[24−27] Moreover, the interfacial doping can adjust the Fermi level (E_F) of the thin film, which may spontaneously form 2DEG with high carrier mobility, a property highly desirable for both fundamental studies and nanoelectronics applications.

In this study, we present a delicate molecular beam epitaxy (MBE) method of epitaxially grown InSe films on an inert graphene substrate by controllable synthesis. The identifications of InSe constitutions are accomplished by both scanning tunneling microscope (STM) and Raman spectroscopic characterizations. The thickness-dependent evolution of the band gap shows an inverse trend for InSe films, while obvious in-gap states emerge only with a thickness larger than 1 TL. Type-I band alignments are visualized between the lateral heterojunctions of InSe films, as long as local lattice imperfections occur, which is interpreted as the strain-modulated band gap within the framework of our density functional theory (DFT) calculations. Interestingly, profiting

from the substrate doping effect, the thinnest InSe film exhibits a highly conductive 2DEG above the conduction band (CB) with strong features of quasiparticle interference (QPI) modulations, a promising characteristic for fabricating field-effect devices and optoelectronic applications with high carrier mobility. Our work demonstrates the highly multifunctional of InSe film with fascinating properties for future optoelectronic and transistor applications, thus can be extended to a variety of 2D vdW materials with heterostructures.

RESULTS AND DISCUSSION

Atomically flat InSe ultrathin films can be epitaxially grown on a graphene substrate by evaporating powdered In$_2$Se$_3$ at 300−350 °C. Figure 1c is a typical STM morphology of InSe films with different thickness, showing straight step edges with an apparent height of 0.85 nm. The surface is Se-terminated with an in-plane lattice constant of 0.40 $\pm$ 0.01 nm, as shown in inset. From the fast Fourier transformation (FFT) of the atomic resolution STM image (Figure 1d), we obtain three sets of diffraction spots in Figure 1e, which are highlighted by the yellow, cyan, and green circles. The calculated distances in real space are 0.40 nm, 1.86 and 3.2 nm, respectively. It is easy to regard the former two as the 1×1-InSe lattice and SiC-6×6 reconstruction from substrate,[28] respectively. The last spatial period represents a Moiré pattern formed from the interferential alignments of the graphene and overlaying InSe films, which are commonly observed in the 2D vdW heterostructures due to the lattice mismatch without considering the interlayer interaction.[29] The 3.2 nm-period is also observed in the STM image of Figure 1d, a result of the superimposition of graphene (13×0.246 nm = 3.2 nm) and InSe (8×0.4 nm = 3.2 nm) lattice. Raman spectroscopy is further performed to measure the phonon vibration modes of epitaxially grown InSe films, as shown in Figure 1f. By comparing to the bulk InSe and In$_2$Se$_3$ crystals, we identify three vibrational modes of MBE-grown InSe films as 112 cm^{-1}, 174 cm^{-1}, and 227 cm^{-1}, consistent with previous studies of A_{1g}^1, E_{2g}^1, and A_{1g}^2, respectively.[9,13,14] The single-phonon
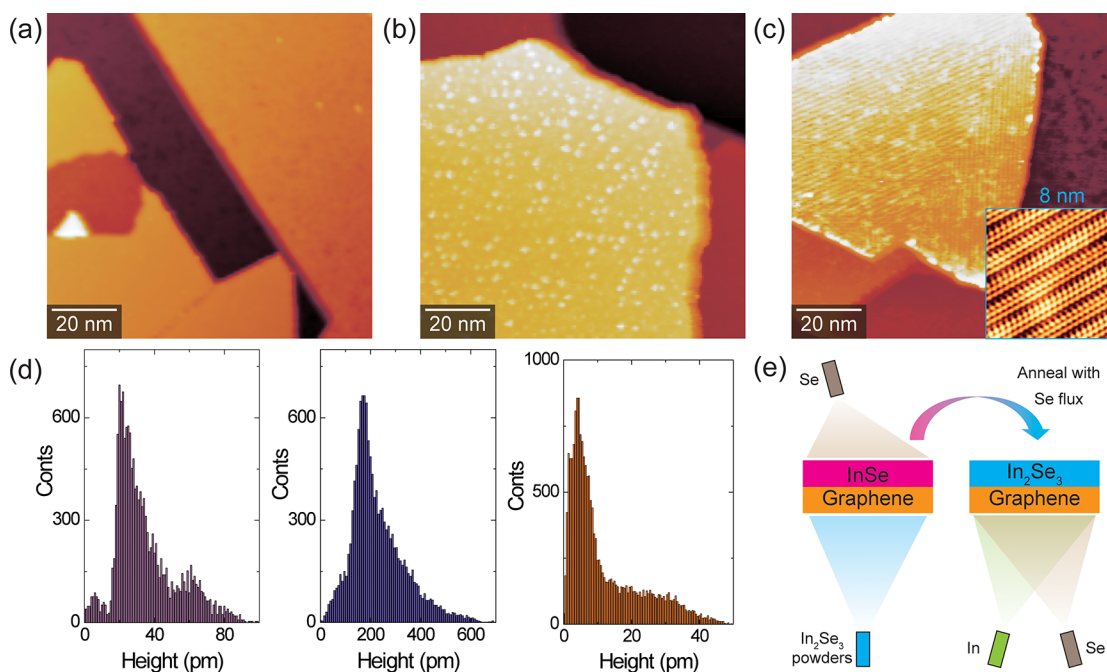
Figure 2. Controlled MBE growth of InSe and In_2Se_3 films. (a)−(c) Topographic images of MBE grown InSe and In_2Se_3 films on a graphene substrate, that is, the as-gown InSe film (a), after Se deposition (b), and further dealt with a postannealed process (c), respectively. All STM images are acquired under conditions: 100×100 nm^2, V_{bias} = +1.5 V, I_t = 10 pA. Inset of (c) is the atomic resolution of In_2Se_3 surface with striped superstructures (8×8 nm^2, V_{bias} = +100 mV, I_t = 100 pA). (d) Height histogram on a 40×40 nm^2 terrace for (a)−(c), giving an average roughness of 37, 208, and 11 pm, respectively. (e) Schematic illustration of the different growth conditions for InSe and In_2Se_3 films, as well as the phase transformation between InSe and In_2Se_3.

vibrations of A_{1g}^1 and A_{1g}^2 originate from the breathing and opposite out-of-plane vibrations of In−Se layers, respectively, and can induce an anomalous magneto-optic effect revealed by recent magneto-Raman measurements.[30] Such spectrum characteristics are highly distinguished between InSe and In_2Se_3 samples, as indicated by the signals of vertical broken cyan lines. Combining with the STM observations of atomic structure, we thus unambiguously confirm the epitaxial growth of InSe films with controlled thickness.

Since the InSe films is synthesized by directly evaporating powdered In_2Se_3 onto the graphene substrate, it is natural to ask the difference between the epitaxial growth of InSe and In_2Se_3 films, as well as their relationship. Starting from the obtained InSe surface that is somewhat rough with substantial defects (Figures 1d and 2a), we expose this surface with a Se flux for 15 min and immediately record its morphology in Figure 2b. Obviously bright protrusions of Se adatoms are visible, randomly distributed on the InSe terrace. Then, we postanneal the sample without Se precursors. The STM image in Figure 2c displays a smoother surface with apparent striped superstructures (inset). Such stripe is a distinctive signature of $β'$-In_2Se_3 that had been widely reported in the bulk crystals,[31] 2D nanoflakes,[32] and 1D nanoribbons,[33] and usually interpreted as local ferroelectric polarization in crystallography,[34,35] which is recently argued to stem from the 2D antiferroelectricity and its competition with 2D ferroelectric ordering.[31] We present a comparison of statistical analysis of height histogram applied over a 40×40 nm^2 terrace in Figure 2d, showing the roughness distribution of each stage. The root-mean-square (RMS) roughness is calculated as 37, 208, and 11 pm, respectively, for the as-grown InSe film, after Se deposition, and further dealing with a postannealed process. Considering the different evaporating process and the phase

transition between InSe and In_2Se_3, we provide a cartoon in Figure 2e to illustrate the different growth conditions required for InSe and In_2Se_3: the In_2Se_3 powder decompose into InSe pieces with Se steams thermally desorbing, only the former one resides on the graphene substrate. The moderately rough surface of InSe film originates from the deficiencies of Se that are mainly seen as holes in the STM image (Figure 1d). After exposure under Se flux, the extra Se adatoms accumulate as clusters and form a disordered surface. With further annealing, the Se adatoms start to coalesce with InSe and develop into In_2Se_3 with continuous films. On the other hand, if both In and Se are evaporated separately, there are sufficient Se atoms to interact with the isolated In atoms, thus can directly crystallize as In_2Se_3 film. Once the In_2Se_3 compound forms, it is stable against further annealing.

The morphologies of the as-grown InSe films (Figure 1c) are comprised of various thicknesses, enabling us to detect their thickness-dependent electronic properties with scanning tunneling spectroscopy (STS) measurements. Typical dI/dV spectra acquired on 1−5 TL InSe films are plotted in Figure 3a, exhibiting clear band gaps. Due to the substrate effect, all InSe films are n-type doped. By increasing the film thickness, the valence band (VB) gradually shifts toward E_F but the CB almost keeps unchanged, giving a decreased band gap size from 1.37 eV of 1 TL to 1.01 eV of 5 TL. Figure 3b summarizes the evolution of the band gap size as a function of film thickness, showing a nearly inverted layer dependence.[36] The values and inverse trend reasonably match well with our first-principles calculations with an overall fluctuation of ∼0.2 eV (Supporting Information (SI) Figure S1), as well as agreeing with previous experimental and theoretical results reported in literature.[9,10,27,37] The sensitive tunability of the band gap via film thickness is commonly observed in 2D vdW materials. In
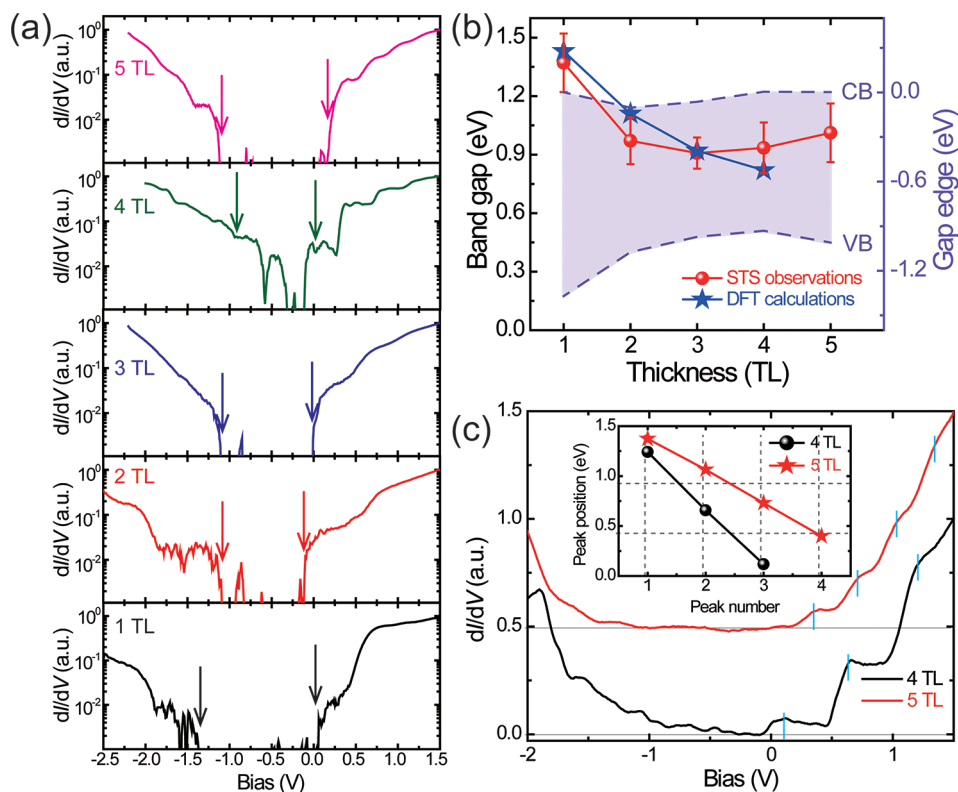
Figure 3. STS characterization of InSe films with different thicknesses. (a) dI/dV spectra taken on 1−5 TL InSe terraces plotted in a logarithmic scale (set point: V_{bias} = +1.5 V, I_t = 100 pA, and V_{mod} = 20 mV). The CB and VB edges are indicated by the colored arrows. (b) Evolution of the CB and VB edges (dashed lines), as well as the band gap size (solid lines) as a function of InSe film thickness for STS observations and theoretical calculations. The error bars are extracted from the statistical minimum and maximum values measured over about five spectra for each layer. (c) A close-up of STS spectra for 4 and 5 TL, showing clear step-like states for the CB regions. The cyan vertical bars indicate the energy positions of each staircase, which are plotted in inset in a linear relationship. Spacing energies of ∼0.56 and 0.33 eV are extracted by linear fitting, respectively, for 4 and 5 TL (set point: V_{bias} = +1.5 V, I_t = 100 pA, and V_{mod} = 20 mV).

contrast to the indirect-to-direct band gap transition in TMDs and black phosphorus with decreased film thickness,[7,8,38] here the band gap in InSe film experiences a crossover from direct to indirect upon reducing layers, as revealed by spatially resolved angular resolved photoemission spectroscopy (ARPES) studies.[39,40]

Intriguingly, two aspects should be noted for the spectra of InSe films. First, the CB brands of STS on both 4 and 5 TL show a sharp increase with a series of steps (Figure 3c), forming staircase-like density of states (DOS). Similar step-like dI/dV character has also been reported by resonant tunneling spectroscopy and photoluminescence excitation measurements in few-layer InSe flakes, which is attributed to the subband structure by the quantum-confined Stark effect.[41] Here by extracting the energy position of each step, we obtain a nicely linear relationship (inset) with average energy intervals of ∼0.56 and 0.33 eV, respectively, for 4 and 5 TL, demonstrating the quantized subbands of quantum well states with confined carriers. Second, by zooming in the scanning energy scales, obvious nonvanishing conductance arises within the band gap for film thickness larger than 1 TL, as displayed in SI Figure S2. As a result, by probing in narrow-energy range, the "U-shaped" landscape of STS spectrum in 1 TL evolves into a "V-shaped" background in 2−5 TL. While all thicknesses of InSe films share similar level of defect density, such in-gap states with pronounced peaks are hardly seen in 1 TL but homogeneously distributed against light defects (spatial extension within ∼1 nm) on 2−5 TL, suggesting no relation between defects and

these in-gap states (SI Figure S3). Together with the absence of peaks in 1 TL and clear QPI patterns for all thicknesses of InSe films, we speculate the defect-induced midgap states, which are expected from theoretical calculations,[24,42] seem unlikely the underlying origin of in-gap peaks. Moreover, the highly conductive 2DES in InSe[21,22] should not be the major contributor by comparing the energy scale: while these states mainly occur below the CB minimum (between −1.2 and 0 eV), the QPI energy range above the CB minimum (>0.2 eV as discussed later).

While the strong quantum confinement of the light effective mass electrons with quantized states (SI Figure S4) may be a plausible mechanism, we speculate that the interlayer coupling should also be a possible candidate considering the prerequisite of thickness >1 TL. Recently, theoretical modellings have proposed emerged excitations inside InSe band gap. Either the interlayer coupling effect is expected to induce pronounced band-edge states in the VB,[43] or moderately electron−phonon interaction can create satellite quasiparticle states near the Fermi energy.[44] In particular, the interlayer coupling has been demonstrated to warp both CB and VB structure of InSe, giving rise to a 2D van Hove singularity that is visible as a sharp low-energy peak in the DOS. Thus, there will form a series of subbands in multiple layers that never exists in 1 TL,[45] resembling what we observe here, which is also similar to the absorption resonances observed in few-layer black phosphorus.[46,47] On the other hand, the emergence of these midgap states should be ascribed
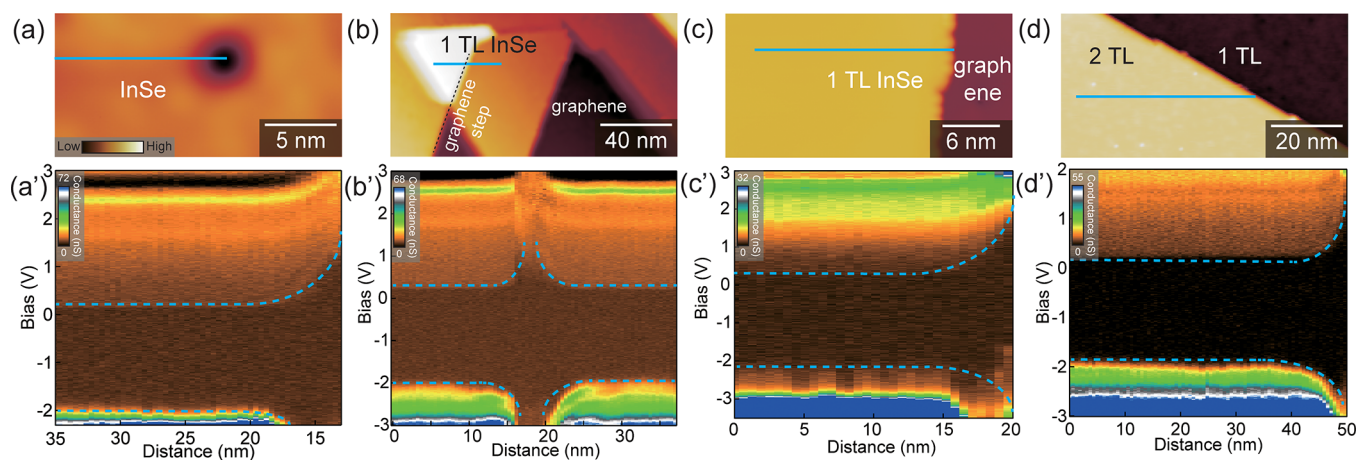
Figure 4. Band gap enhancement near structural imperfections with Type-I band alignment in InSe films. (a)−(d) Typical STM images for 1 TL InSe surface containing an isolated defect (a, 20×10 nm^2, V_{bias} = +0.5 V, I_t = 30 pA), 1 TL across graphene step (b, 200×100 nm^2, V_{bias} = +3.0 V, I_t = 10 pA), step boundary between 1 TL InSe and graphene substrate (c, 30×15 nm^2, V_{bias} = +1.5 V, I_t = 10 pA), step edge between 1 and 2 TL InSe films (d, 80×40 nm^2, V_{bias} = +2.0 V, I_t = 10 pA), respectively. (a')−(d') 2D plot of tunneling spectra measured along the cyan line in (a)−(d), respectively. The dashed cyan curves are guides for the eye following the trends of CB and VB when approaching the boundaries. Set points are V_{bias} = +3.0 V for (a')−(c'), V_{bias} = +2.0 V for (d'), I_t = 100 pA, and V_{mod} = 30 mV.
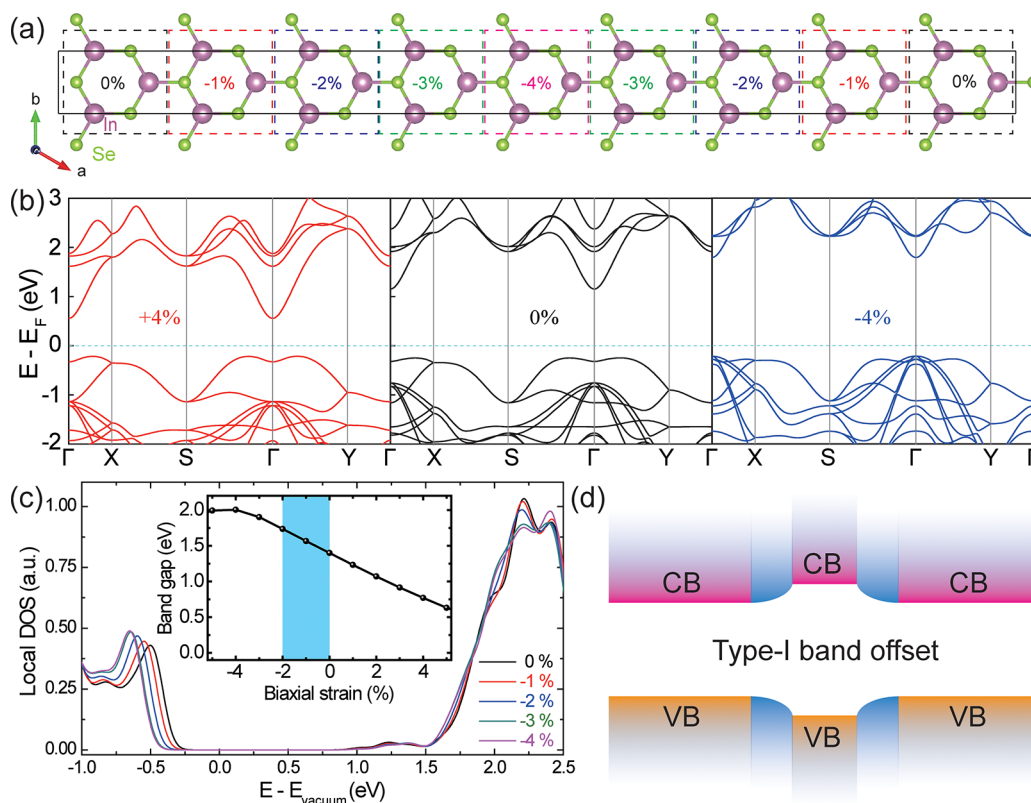
Figure 5. Theorical calculated band gap evolution for InSe films under various strain effect. (a) Top view of calculated atomic configuration for the 1 TL InSe. Different uniaxial strain is applied by varying the pristine lattice constant, which are marked as the dashed squares. (b) Band structures of 1 TL InSe with biaxial strain of +4%, 0%, and −4%, respectively. The Fermi level is set as zero by the dashed cyan line. (c) Calculated local DOS for the top Se atoms (the same colors labeled in (a)) of different level of compressive strain, respectively. Inset is the biaxial strain dependence of the band gap size on 1 TL InSe. The light cyan shadow indicates the possible strained region of −2% in experiments. (d) An animated illustration of type-I band offset across the heterojunction, where magenta (orange) shadows indicate the CB (VB) and cyan regions stand for the band alignments.

to some inherent properties of InSe itself rather than the external factors (SI Figure S5). We cannot exclude contributions from other mechanisms, such as the exciton characters due to the Coulomb interaction,[17] or certain vibrational phonon modes by the electron−phonon coupling.[30]

Nevertheless, the exact origin of these midgap states still remains unsolved deserving further investigations, and probably extends additional degree of freedom to tune the exotic electronic properties of 2D InSe.
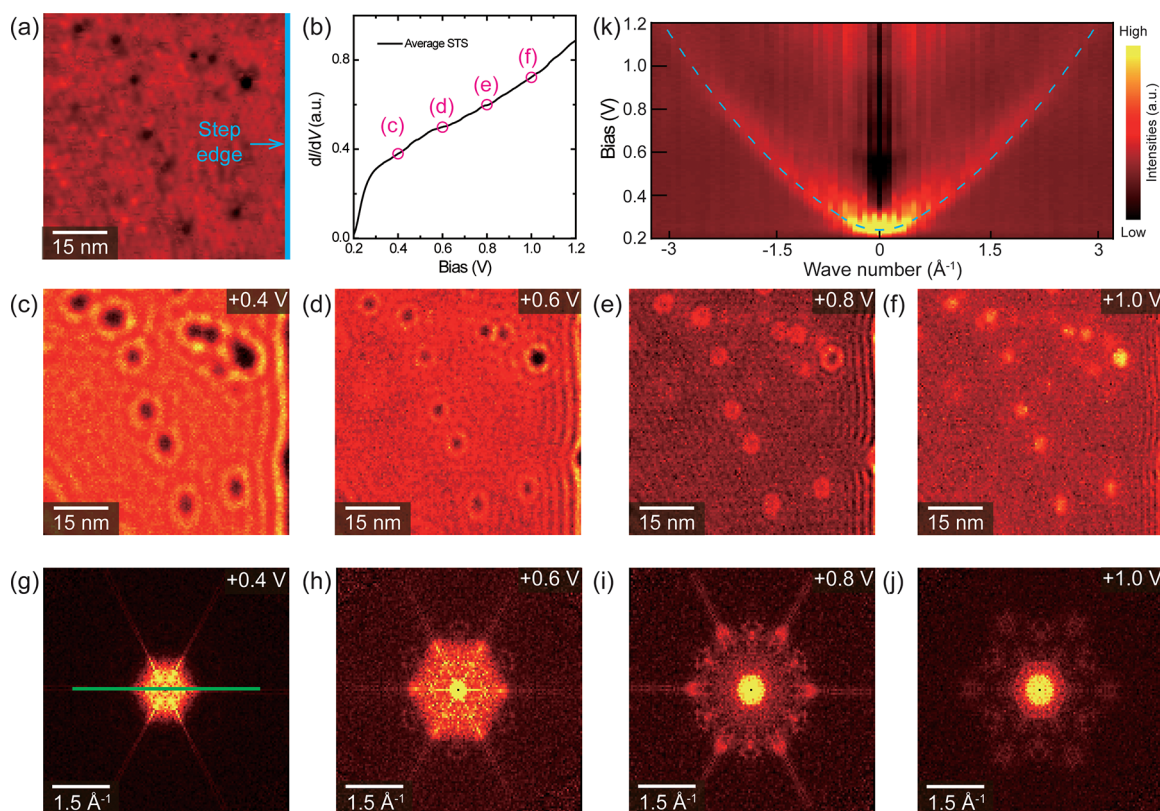
Figure 6. 2DEG in 1 TL InSe films revealed by QPI. (a) STM images of 1TL InSe surface containing both defects and step, with the latter one indicated by a vertical cyan line (67.8×67.8 nm^2, V_{bias} = +1.2 V, I_t = 100 pA). (b) Average STS over the InSe surface in (a). (c)−(f) Real-space conductance mappings acquired over the same area of (a) at bias energies of 0.4, 0.6, 0.8, and 1.0 V, respectively. The selected energies are also displayed in (b). (g)−(j) The corresponding 2D FFTs of (c)−(f). A 6-fold symmetrization is implemented. (k) 2D plot of QPI peak along the green line in (g), showing the energy dispersion relation of CB. A parabolic fitting is overlaid by a dashed cyan curve.

To gain deeper insight into the band gap nature of InSe films, we investigate the variation of the electronic structure under various crystalline perturbations. The aforementioned observations in SI Figures S2 and S3 demonstrate that the DOS of InSe films is rather homogeneous even though the surface is disordered with light defects. We thus concentrate on the extended disorders (defects or edge boundaries) over 10 nm-range. As is shown in Figure 4a−d, four representative situations are chosen for comparison: an extended defect (a), continuous 1 TL InSe across an underlying step of the graphene substrate (b), step edge between 1 TL InSe and graphene substrate (c), and step edge between 1 and 2 TL InSe films (d). Their corresponding tunneling spectra acquired along the cyan lines are plotted in Figure 4a'−d', respectively, exhibiting similar behaviors: Upon approaching the defect or edges, the variations of CB and VB shoulders behave in the opposite direction, that is, while the CB shoulder moves to higher energies, the VB shoulder shifts toward lower energies. These lead to strong upward and downward band bending when crossing the interface, respectively, as illustrated by the dashed cyan lines. For instance, as is seen in Figure 4a', the shoulder of the CB (VB) on the 1 TL InSe terrace far away from the defect locates at ∼0.2 (−2.0) eV, but starts to bend at a distance of ∼5 nm away from the edge, and gradually shifts to ∼0.5 (−2.1) eV right at the edge, thus giving a much larger band gap on the extended defect, ∼0.4 eV enhancement comparing to the pristine band gap of 1 TL. Similar phenomena occur in the vicinity of graphene step, InSe/ graphene, and 2 TL/1 TL step boundaries, with significantly

increase of 0.3, 0.5, and 0.4 eV at the edges, respectively. The specific comparisons of point spectra can be found in SI Figure S6. It is worth mentioning that the band gap sizes shown in 2D plots are globally larger than in Figure 3. This is due to different methods for determining the gap edges (SI Figures S6−S8), which, however, do not influence the trends of the band bending behaviors. We also note that the spatial extensions of bending are all on the order of 10 nm, and the unperturbed or "bulk" band structures are spatially homogeneous. Such large spatial extension should not be induced by trivial edge states or conventional lattice reconstruction, which is usually more localized with extended length smaller than 2 nm. Although we fail to obtain the exactly atomic arrangement in the vicinity of disorders, we find the large modification of band gap (>20%) commonly exist irrespective of film thickness, even though sometimes the band bending only occurs on the upper terrace of atomic step, but almost disappears on the lower side, as displayed in SI Figure S9.

Apparently, all the enhancements of band gap are universal and closely related to certain structural perturbations, implying the lattice deformation should play a fundamental role in the modification of band structure. We thus employ the first-principles calculations to systematically simulate the effect of in-plane strain, which is more extended compared to local lattice distortion, on single TL InSe. As indicated in Figure 5a, we construct a compressed supercell spliced by nine unit-cells, where variant biaxial strain is applied by varying the in-plane lattice constant with fully relaxed Se and In atomic positions. Here, the compression is not uniform but changes continu-

ously along one direction, with the maximum (−4%) sitting in the middle of the sample. Figure 5b presents the calculated electronic structures for a tensile (compressive) strain of 4% (−4%) with respect to the unstrained case. Clearly, compared to the pristine 1 TL InSe of 1.40 eV, it keeps indirectly semiconducting with a decreased band gap of 0.77 eV (−45%) under a small (+4%) in-plane tensile, but converts into a direct semiconductor with an enhanced band gap of 2.0 eV (+44%) if only a −4% compressive strain is applied. This apparent modification is accompanied by the acuminous movement of VB maximum, as well as the CB minimum at Γ point. In Figure 5c, we compare the calculated local DOS of topmost In atoms from different parts of the simulated sample (Figure 5a) and confirm both shift of VB and CB under different compressive strain. Inset in Figure 5c plots the variation of band gap under different biaxial strain. Except for the much large strain that may induce exotic phase,[48] the band gap monotonously increases with decreasing the tensile strain, associated with an indirect-to-direct bandgap transition. Considering our ∼0.5 eV (+22%) enhancement of gap size, we speculate a ∼2% compressive strain near the defect or crystalline boundaries of the epitxial InSe films by lattice deformation (shadowed region). As a result, the band offset of the enhanced gap across the heterojunctions leads to the type-I band alignment in InSe films, which is schematically sketched in Figure 5d. As is well-known, the band bending effect in the semiconducting heterostructures usually originates from the discrepancy in the work function of different layers, associated with charge accumulation or depletion taking place at the contacting regions. Considering that the graphene/SiC substrates share the same work function, the distinct sensitive dependence of the band bending for InSe films indicate that carriers are more easily to be trapped at defects/edges.

Finally, considering the electron doping effect of the graphene/SiC substrate (Figure 3a), the Fermi level of InSe films can be likely shifted close to or even above the confinement-quantized CB, thus giving rise to the formation of 2DES with high mobility down to 1 TL. As depicted in Figure 6, we directly demonstrate the characteristics of 2DES in real space by visualizing the band dispersions via the spectroscopic imaging scattering properties. In the field of view for a 1 TL InSe surface, the terminated terrace contains plenty of defects and step boundaries (Figure 6a). The local DOS thus spatially varies depending on its distance to the step edge or defects, forming modulated QPI patterns. Figure 6b is the average STS over the InSe surface in Figure 6a. As indicated in Figures 6c−f, the real-space conductance mappings acquired over the same area can be resolved at selected bias energies of 0.4, 0.6, 0.8, and 1.0 V, respectively. Clear standing-wave patterns are presented in the vicinity of defects and step edge, whose wavelength gradually decreases with increasing energies. 2D FFTs are performed in Figure 6g−j to further provide momentum-resolved information in the concerning energy range, especially for the energies above E_F that are inaccessible in the ARPES measurements.[39,40] By tracing the energy-dependent interference peak along the green line in Figure 6g, we can easily extract the energy dispersion relation of CB, as plotted in Figure 6k. A positive parabolic is well resolved with a high-intensity bottom at ∼250 meV (SI Figures S7 and S8), indicating the minimum of CB that is conformable with the point spectrum (Figure 6b). We fit the dispersion by a parabolic function in a dashed cyan curve, and calculate the Fermi velocity (in the momentum space, $v_F = 1/\hbar \times d\varepsilon/dk$

with $\hbar$ the reduced Planck constant) as 0.53 eV·Å (or 0.81 × 10^5 m·s⁻¹) at relatively high energies (0.8−1.2 eV). The effective mass ($m^* = \hbar^2 \times d^2k/d\varepsilon^2$) of the electron in CB is determined as 0.27 m_0, with m_0 the free electron mass. Our result is the same order of magnitude as that reported values of 0.14−0.33 m_0 by ARPES and transport measurements,[15,21,39,40] confirming the low carrier effective mass and ultrahigh mobility in InSe films.

CONCLUSIONS

In summary, we have developed controllable synthesis of epitaxial InSe films by a delicate MBE method. STM/STS is demonstrated as a felicitous tool to determine the morphological and electronic characterizations with variant film thicknesses down to the single layer limit, verifying an inversely proportional band gap to the film thickness. We illustrate the type-I band alignments of InSe films under various lattice imperfections with much enhanced band gap nearby the boundaries, which is understood as the modulation of electronic and band structure by the strain effect. Finally, we demonstrate that the substrate doping benefits the electrons self-forming 2DES with a small effective mass of 0.27 m_0 in the 2D limit, as revealed by the visualization of QPI patterns. Our observations of intriguing properties in 2D InSe films provide enticing possibilities for flexible utilization enabling extensive varieties of applications, such as light emitting diodes based on type-I heterostructures,[49] controlling/trapping localization of charges with high mobilities, or long-lived interlayer excitons.[50]

METHODS

MBE Growth. All samples were grown in a customized MBE chamber with a base pressure 5 × 10⁻¹⁰ mbar.[51] Prior to growth, a uniform graphene-covered 6H-SiC(0001) substrate was prepared in a ultrahigh vacuum chamber. After being degassed at 600 °C for 3 h, the SiC wafer was annealed at 950 °C under a Si flux for five cycles, then becoming atomically flat terminated with graphene by flashing to 1400 °C for 10 min. High-purity of In_2Se_3 powders (99.99%) were evaporated from a heated crucible onto the prepared graphene substrate at 300−350 °C, resulting in epitaxial InSe films. For the growth of In_2Se_3 films, separated In (99.999%) and Se (99.999%) sources were simultaneously coevaporated from two homemade thermal effusions onto the substrate, whose temperature was held at 330 °C. During the growth, the In:Se flux ratio was estimated as ∼1:8, both controlled by the temperatures of In (620 °C) and Se (150 °C) sources. After growth, the samples were annealed at the growth temperature for 10 min with or without a Se overflux, which mainly enhances the quality of the films but do not cause any phase transition (checked by STM measurements).

STM/STS Measurements. The STM/STS measurements were conducted on a Unisoku STM system at 4.5 K.[52] An electrochemically etched W tip was cleaned by e-beam heating and calibrated on a standard Ag(111) sample before all measurements. All topographic images were taken in a constant-current mode, and the tunneling dI/dV spectra and conductance mappings were acquired by standard lock-in technique with modulation voltage frequency of 983 Hz. The amplitude of modulation voltage was given in the figure captions for each spectrum.

Raman Characterization. For *ex situ* Raman measurements, the MBE-grown films were protected with ∼20 nm amorphous Se capping layers against air degradation. The Raman spectra were carried out at room temperature by using a Horiba microRaman system (Labram HR Evolution). The wavelength of the laser excitation was 633 nm with on-sample power at around 100 μW.

Theoretical Calculations. Electronic properties were studied theoretically by performing DFT calculations using the Vienna *ab initio* Simulation Package (VASP), which implemented the projected

augmented wave method.[53−55] First, we obtained lattice constants of unit cell by the process of total energy minimization. As for monolayer InSe, the vacuum space of at least 15 Å was introduced in the directions perpendicular to the monolayer to avoid spurious interactions between periodic supercell images. To apply uniaxial and biaxial strain, we changed the lattice constant of unit cell and make full relaxation of atomic position only. To this end, we used generalized gradient approximation (GGA) in combination with ultrasoft pseudopotentials,[55] in which $4d^{10}5s^25p^1$ electrons of In, $4s^24p^4$ electrons of Se were treated as valent. The energy cutoff of 500 eV was set for a plane-wave basis. The reciprocal space was sampled by a uniform $(15 \times 15 \times 1)$ **k**-point mesh. All atomic positions were fully relaxed using the conjugated gradient method until the Hellmann−Feynman force on each atom was less than 0.01 eV/Å. The convergence for energy was chosen as 10^{-6} eV between two steps.[56] For the large supercell shown in Figure 5a we chose the energy cutoff as 300 eV, and sampled the reciprocal space by a uniform $(3 \times 9 \times 1)$ **k**-point mesh. Besides that, we took $5s^25p^1$ instead of $4d^{10}5s^25p^1$ as valent for In element since most of electronic states in the vicinity of the Fermi energy were contributed by s- and p-orbitals.

ASSOCIATED CONTENT

🅢ⁱ Supporting Information

The Supporting Information is available free of charge at https://pubs.acs.org/doi/10.1021/acsnano.1c03724.

> Figures of layer-dependent band structure for 1−4 TL InSe; figure of STS spectra in a linear scale for 1−5 TL InSe; figure of STS linecuts across various defects; figure of STS spectra with spatial homogeneity; figure of 2D plot of STS spectra across a strained defect; figure of STS spectra across various defects/step boundaries; figure of comparison for the QPI observations and the STS in determining the band gap size; figure of comparison for the onset and shoulder of band gap edge; figure of band bending across different layer steps (PDF)

AUTHOR INFORMATION

Corresponding Authors

Wenhao Zhang − School of Physics and Wuhan National High Magnetic Field Center, Huazhong University of Science and Technology, Wuhan 430074, China; ⓞ orcid.org/0000-0003-2386-0305; Email: wenhaozhang@hust.edu.cn

Ying-Shuang Fu − School of Physics and Wuhan National High Magnetic Field Center, Huazhong University of Science and Technology, Wuhan 430074, China; ⓞ orcid.org/0000-0001-7876-2812; Email: yfu@hust.edu.cn

Authors

Zhimo Zhang − School of Physics and Wuhan National High Magnetic Field Center, Huazhong University of Science and Technology, Wuhan 430074, China

Yuan Yuan − School of Physics and Wuhan National High Magnetic Field Center, Huazhong University of Science and Technology, Wuhan 430074, China

Weiqing Zhou − Key Laboratory of Artificial Micro- and Nano-structures of Ministry of Education and School of Physics and Technology, Wuhan University, Wuhan 430072, China

Chen Chen − International Center for Quantum Design of Functional Materials (ICQD), Hefei National Laboratory for Physical Science at the Microscale, and Synergetic Innovation Center of Quantum Information and Quantum Physics and Key Laboratory of Strongly-Coupled Quantum Matter

Physics, Chinese Academy of Sciences, Department of Physics, University of Science and Technology of China, Hefei, Anhui 230026, China

Shengjun Yuan − Key Laboratory of Artificial Micro- and Nano-structures of Ministry of Education and School of Physics and Technology, Wuhan University, Wuhan 430072, China; ⓞ orcid.org/0000-0001-6208-1502

Hualing Zeng − International Center for Quantum Design of Functional Materials (ICQD), Hefei National Laboratory for Physical Science at the Microscale, and Synergetic Innovation Center of Quantum Information and Quantum Physics and Key Laboratory of Strongly-Coupled Quantum Matter Physics, Chinese Academy of Sciences, Department of Physics, University of Science and Technology of China, Hefei, Anhui 230026, China; ⓞ orcid.org/0000-0001-5869-9553

Complete contact information is available at:
https://pubs.acs.org/10.1021/acsnano.1c03724

Notes

The authors declare no competing financial interest.

REFERENCES

(1) Geim, A. K.; Grigorieva, I. V. van der Waals Heterostructures. *Nature* **2013**, *499*, 419−425.

(2) Xi, X.; Zhao, L.; Wang, Z.; Berger, H.; Forro, L.; Shan, J.; Mak, K. F. Strongly Enhanced Charge-Density-Wave Order in Monolayer NbSe₂. *Nat. Nanotechnol.* **2015**, *10*, 765−769.

(3) Tong, Q.; Yu, H.; Zhu, Q.; Wang, Y.; Xu, X.; Yao, W. Topological Mosaics in Moiré Superlattices of van der Waals Heterobilayers. *Nat. Phys.* **2017**, *13*, 356−362.

(4) Chang, K.; Liu, J.-W.; Lin, H.- C.; Wang, N.; Zhao, K.; Zhang, A.-M.; Jin, F.; Zhong, Y.; Hu, X.-P.; Duan, W.-H.; Zhang, Q.-M.; Fu, L.; Xue, Q.-K.; Chen, X.; Ji, S.-H. Discovery of Robust In-Plane Ferroelectricity in Atomic-Thick SnTe. *Science* **2016**, *353*, 274−278.

(5) Huang, B.; Clark, G.; Navarro-Moratalla, E.; Klein, D. R.; Cheng, R.; Seyler, K. L.; Zhong, D.; Schmidgall, E.; McGuire, M. A.; Cobden, D. H.; Yao, W.; Xiao, D.; Jarillo-Herrero, P.; Xu, X. Layer-Dependent Ferromagnetism in a van der Waals Crystal Down to the Monolayer Limit. *Nature* **2017**, *546*, 270−273.

(6) Molle, A.; Goldberger, J.; Houssa, M.; Xu, Y.; Zhang, S.-C.; Akinwande, D. Buckled Two-Dimensional Xene Sheets. *Nat. Mater.* **2017**, *16*, 163−169.

(7) Anasori, B.; Lukatskaya, M. R.; Gogotsi, Y. 2D Metal Carbides and Nitrides (MXenes) for Energy Storage. *Nat. Rev. Mater.* **2017**, *2*, 16098.

(8) Carvalho, A.; Wang, M.; Zhu, X.; Rodin, A. S.; Su, H.; Castro Neto, A. H. Phosphorene: From Theory to Applications. *Nat. Rev. Mater.* **2016**, *1*, 16061.

(9) Song, C.; Huang, S.; Wang, C.; Luo, J.; Yan, H. The Optical Properties of Few-Layer InSe. *J. Appl. Phys.* **2020**, *128*, 060901.

(10) Han, G.; Chen, Z.-G.; Drennan, J.; Zou, J. Indium Selenides: Structural Characteristics, Synthesis and Their Thermoelectric Performances. *Small* **2014**, *10*, 2747−2765.

(11) Poh, S. M.; Tan, S.-J.-R.; Wang, H.; Song, P.; Abidi, I. H.; Zhao, X.; Dan, J.; Chen, J.; Luo, Z.; Pennycook, S. J.; Castro Neto, A. H.; Loh, K. P. Molecular-Beam Epitaxy of Two-Dimensional In$_2$Se$_3$ and Its Giant Electroresistance Switching in Ferroresistive Memory Junction. *Nano Lett.* **2018**, *18*, 6340−6346.

(12) Sun, Y.; Li, Y.; Li, T.; Biswas, K.; Patane, A.; Zhang, L. New Polymorphs of 2D Indium Selenide with Enhanced Electronic Properties. *Adv. Funct. Mater.* **2020**, *30*, 2001920.

(13) Tao, X.; Gu, Y. Crystalline-Crystalline Phase Transformation in Two-Dimensional In$_2$Se$_3$ Thin Layers. *Nano Lett.* **2013**, *13*, 3501−3505.

(14) Hao, Q.; Liu, J.; Wang, G.; Chen, J.; Gan, H.; Zhu, J.; Ke, Y.; Chai, Y.; Lin, J.; Zhang, W. Surface-Modified Ultrathin InSe Nanosheets with Enhanced Stability and Photoluminescence for High-Performance Optoelectronics. *ACS Nano* **2020**, *14*, 11373−11382.

(15) Lei, S.-D.; Ge, L.-H.; Najmaei, S.; George, A.; Kappera, R.; Lou, J.; Chhowalla, M.; Yamaguchi, H.; Gupta, G.; Vajtai, R.; Mohite, A. D.; Ajayan, P. M. Evolution of the Electronic Band Structure and Efficient Photo-Detection in Atomic Layers of InSe. *ACS Nano* **2014**, *8*, 1263−1272.

(16) Brotons-Gisbert, M.; Proux, R.; Picard, R.; Andres-Penares, D.; Branny, A.; Molina-Sanchez, A.; Sanchez-Royo, J. F.; Gerardot, B. D. Out-of-Plane Orientation of luminescent Excitons in Two-Dimensional Indium Selenide. *Nat. Commun.* **2019**, *10*, 3913.

(17) Shubina, T. V.; Desrat, W.; Moret, M.; Tiberj, A.; Briot, O.; Davydov, V. Y.; Platonov, A. V.; Semina, M. A.; Gil, B. InSe as a Case between 3D and 2D Layered Crystals for Excitons. *Nat. Commun.* **2019**, *10*, 3479.

(18) Ming, W.; Wang, Z.-F.; Zhou, M.; Yoon, M.; Liu, F. Formation of Ideal Rashba States on Layered Semiconductor Surfaces Steered by Strain Engineering. *Nano Lett.* **2016**, *16*, 404−409.

(19) Premasiri, K.; Radha, S. K.; Sucharitakul, S.; Kumar, U. R.; Sankar, R.; Chou, F.-C.; Chen, Y.-T.; Gao, X.-P.-A. Tuning Rashba Spin-Orbit Coupling in Gated Multilayer InSe. *Nano Lett.* **2018**, *18*, 4403−4408.

(20) Ubrig, N.; Ponomarev, E.; Zultak, J.; Domaretskiy, D.; Zolyomi, V.; Terry, D.; Howarth, J.; Gutierrez-Lezama, I.; Zhukov, A.; Kudrynskyi, Z. R.; Kovalyuk, Z. D.; Patane, A.; Taniguchi, T.; Watanabe, K.; Gorbachev, R. V.; Fal'ko, V. I.; Morpurgo, A. F. Design of van der Waals Interfaces for Broad-Spectrum Optoelectronics. *Nat. Mater.* **2020**, *19*, 299−304.

(21) Bandurin, D. A.; Tyurnina, A. V.; Yu, G. L.; Mishchenko, A.; Zolyomi, V.; Morozov, S. V.; Kumar, R. K.; Gorbachev, R. V.; Kudrynskyi, Z. R.; Pezzini, S.; Kovalyuk, Z. D.; Zeitler, U.; Novoselov, K. S.; Patane, A.; Eaves, L.; Grigorieva, I. V.; Fal'ko, V. I.; Geim, A. K.; Cao, Y. High Electron Mobility, Quantum Hall Effect and Anomalous Optical Response in Atomically Thin InSe. *Nat. Nanotechnol.* **2017**, *12*, 223−227.

(22) Kudrynskyi, Z. R.; Bhuiyan, M. A.; Makarovsky, O.; Greener, J. D. G.; Vdovin, E. E.; Kovalyuk, Z. D.; Cao, Y.; Mishchenko, A.; Novoselov, K. S.; Beton, P. H.; Eaves, L.; Patanè, A. Giant Quantum Hall Plateau in Graphene Coupled to an InSe van der Waals Crystal. *Phys. Rev. Lett.* **2017**, *119*, 157701.

(23) Wei, T.-R.; Jin, M.; Wang, Y.-C.; Chen, H.-Y.; Gao, Z. Q.; Zhao, K.-P.; Qiu, P.-F.; Shan, Z.-W.; Jiang, J.; Li, R.-B.; Chen, L.-D.; He, J.; Shi, X. Exceptional Plasticity in the Bulk Single-Crystalline van der Waals Semiconductor InSe. *Science* **2020**, *369*, 542−545.

(24) Li, Y.; Wang, T.; Wu, M.; Cao, T.; Chen, Y.; Sankar, R.; Ulaganathan, R. K.; Chou, F.; Wetzel, C.; Xu, C.-Y.; Louie, S. G.; Shi, S.-F. Ultrasensitive Tunability of the Direct Bandgap of 2D InSe Flakes *via* Strain Engineering. *2D Mater.* **2018**, *5*, 021002.

(25) Wu, M.; Shi, J.-J.; Zhang, M.; Ding, Y.-M.; Wang, H.; Cen, Y.-l.; Lu, J. Enhancement of Photoluminescence and Hole Mobility in 1- to 5-Layer InSe Due to the Top Valence-Band Inversion: Strain Effect. *Nanoscale* **2018**, *10*, 11441.

(26) Song, C.; Fan, F.; Xuan, N.; Huang, S.; Wang, C.; Zhang, G.; Wang, F.; Xing, Q.; Lei, Y.; Sun, Z. Drastic Enhancement of the Raman Intensity in Few-Layer InSe by Uniaxial Strain. *Phys. Rev. B: Condens. Matter Mater. Phys.* **2019**, *99*, 195414.

(27) Zhao, Q.; Wang, T.; Frisenda, R.; Castellanos-Gomez, A. Giant Piezoresistive Effect and Strong Bandgap Tunability in Ultrathin InSe Upon Biaxial Strain. *Adv. Sci.* **2020**, *7*, 2001645.

(28) Peng, L.; Zhao, J.; Cai, M.; Hua, G.-Y.; Liu, Z.-Y.; Xia, H.-N.; Yuan, Y.; Zhang, W.-H.; Xu, G.; Zhao, L.-X.; Zhu, Z.-W.; Xiang, T.; Fu, Y.-S. Mott Phase in a van der Waals Transition-Metal Halide at Single-Layer Limit. *Phys. Rev. Res.* **2020**, *2*, 023264.

(29) Peng, L.; Qiao, J.; Xian, J.-J.; Pan, Y.; Ji, W.; Zhang, W.; Fu, Y.-S. Unusual Electronic States and Superconducting Proximity Effect of Bi Films Modulated by a NbSe$_2$ Substrate. *ACS Nano* **2019**, *13*, 1885−1892.

(30) Fu, W.; Zhao, X.; Wang, K.; Chen, Z.; Leng, K.; Fu, D.; Song, P.; Wang, H.; Deng, L.; Pennycook, S. J.; Zhang, G.; Peng, B.; Loh, K. P. An Anomalous Magneto-Optic Effect in Epitaxial Indium Selenide Layers. *Nano Lett.* **2020**, *20*, 5330−5338.

(31) Xu, C.; Chen, Y.; Cai, X.; Meingast, A.; Guo, X.; Wang, F.; Lin, Z.; Lo, T.-W.; Maunders, C.; Lazar, S.; Wang, N.; Lei, D.; Chai, Y.; Zhai, T.; Luo, X.; Zhu, Y. Two-Dimensional Antiferroelectricity in Nanostripe-Ordered In$_2$Se$_3$. *Phys. Rev. Lett.* **2020**, *125*, 047601.

(32) Lin, M.; Wu, D.; Zhou, Y.; Huang, W.; Jiang, W.; Zheng, W.; Zhao, S.; Jin, C.; Guo, Y.; Peng, H.; Liu, Z. Controlled Growth of Atomically Thin In$_2$Se$_3$ Flakes by van der Waals Epitaxy. *J. Am. Chem. Soc.* **2013**, *135*, 13274−13277.

(33) Lai, K.-J.; Peng, H.-L.; Kundhikanjana, W.; Schoen, D. T.; Xie, C.; Meister, S.; Cui, Y.; Kelly, M. A.; Shen, Z.-X. Nanoscale Electronic Inhomogeneity in In$_2$Se$_3$ Nanoribbons Revealed by Microwave Impedance Microscopy. *Nano Lett.* **2009**, *9*, 1265−1269.

(34) Zheng, C.-X.; Yu, L.; Zhu, L.; Collins, J. L.; Kim, D.; Lou, Y.-D.; Xu, C.; Li, M.; Wei, Z.; Zhang, Y.-P.; Edmonds, M. T.; Li, S.-Q.; Seidel, J.; Zhu, Y.; Liu, J.-Z.; Tang, W.-X.; Fuhrer, M. S. Room Temperature in-Plane Ferroelectricity in van der Waals In$_2$Se$_3$. *Sci. Adv.* **2018**, *4*, No. eaar7720.

(35) Xiao, J.; Zhu, H.; Wang, Y.; Feng, W.; Hu, Y.; Dasgupta, A.; Han, Y.; Wang, Y.; Muller, D. A.; Martin, L. W.; Hu, P.; Zhang, X. Intrinsic Two-Dimensional Ferroelectricity with Dipole Locking. *Phys. Rev. Lett.* **2018**, *120*, 227601.

(36) Demirci, S.; Avazlı, N.; Durgun, E.; Cahangirov, S. Structural and Electronic Properties of Monolayer Group III Monochalcogenides. *Phys. Rev. B: Condens. Matter Mater. Phys.* **2017**, *95*, 115409.

(37) Lv, Q.; Yan, F.; Mori, N.; Zhu, W.; Hu, C.; Kudrynskyi, Z. R.; Kovalyuk, Z. D.; Patanè, A.; Wang, K. Interlayer Band-to-Band Tunneling and Negative Differential Resistance in van der Waals BP/InSe Field-Effect Transistors. *Adv. Funct. Mater.* **2020**, *30*, 1910713.

(38) Bradley, A. J.; Ugeda, M. M.; da Jornada, F. H.; Qiu, D. Y.; Ruan, W.; Zhang, Y.; Wickenburg, S.; Riss, A.; Lu, J.; Mo, S.-K.; Hussain, Z.; Shen, Z.-X.; Louie, S. G.; Crommie, M. F. Probing the Role of Interlayer Coupling and Coulomb Interactions on Electronic Structure in Few-Layer MoSe$_2$ Nanostructures. *Nano Lett.* **2015**, *15*, 2594−2599.

(39) Hamer, M. J.; Zultak, J.; Tyurnina, A. V.; Zólyomi, V.; Terry, D.; Barinov, A.; Garner, A.; Donoghue, J.; Rooney, A. P.; Kandyba, V.; Giampietri, A.; Graham, A.; Teutsch, N.; Xia, X.; Koperski, M.; Haigh, S. J.; Fal'ko, V. I.; Gorbachev, R. V.; Wilson, N. R. Indirect to Direct Gap Crossover in Two-Dimensional InSe Revealed by Angle-Resolved Photoemission Spectroscopy. *ACS Nano* **2019**, *13*, 2136−2142.

(40) Kibirev, I. A.; Matetskiy, A. V.; Zotov, A. V.; Saranin, A. A. Thickness-Dependent Transition of the Valence Band Shape from Parabolic to Mexican-Hat-Like in the MBE Grown InSe Ultrathin Films. *Appl. Phys. Lett.* **2018**, *112*, 191602.

(41) Zultak, J.; Magorrian, S. J.; Koperski, M.; Garner, A.; Hamer, M. J.; Tóvári, E.; Novoselov, K. S.; Zhukov, A. A.; Zou, Y.; Wilson, N. R.; Haigh, S. J.; Kretinin, A. V.; Fal'ko, V. I.; Gorbachev, R. Ultra-Thin van der Waals Crystals as Semiconductor Quantum Wells. *Nat. Commun.* **2020**, *11*, 125.

(42) Zhao, Q.; Frisenda, R.; Wang, T.; Castellanos-Gomez, A. InSe: A Two-Dimensional Semiconductor with Superior Flexibility. *Nanoscale* **2019**, *11*, 9845−9850.

(43) Sun, Y.; Luo, S.; Zhao, X.-G.; Biswas, K.; Li, S.-L.; Zhang, L. InSe: a Two-Dimensional Material with Strong Interlayer Coupling. *Nanoscale* **2018**, *10*, 7991−7998.

(44) Lugovskoi, A. V.; Katsnelson, M. I.; Rudenko, A. N. Strong Electron-Phonon Coupling and Its Influence on the Transport and Optical Properties of Hole-Doped Single-Layer InSe. *Phys. Rev. Lett.* **2019**, *123*, 176401.

(45) Li, W.; Poncé, S.; Giustino, F. Dimensional Crossover in the Carrier Mobility of Two-Dimensional Semiconductors: The Case of InSe. *Nano Lett.* **2019**, *19*, 1774−1781.

(46) Li, L.; Kim, J.; Jin, C.; Ye, G.-J.; Qiu, D.-Y.; da Jornada, F. H.; Shi, Z.; Chen, L.; Zhang, Z.; Yang, F.; Watanabe, K.; Taniguchi, T.; Ren, W.; Louie, S. G.; Chen, X. H.; Zhang, Y.; Wang, F. Direct Observation of the Layer-Dependent Electronic Structure in Phosphorene. *Nat. Nanotechnol.* **2017**, *12*, 21−25.

(47) Zhang, Gu; Huang, S.; Chaves, A.; Song, C.; Ozcelik, V. O.; Low, T.; Yan, H. Infrared Fingerprints of Few-Layer Black Phosphorus. *Nat. Commun.* **2017**, *8*, 14071.

(48) Hu, T.; Zhou, J.; Dong, J. Strain Induced New Phase and Indirect-Direct Band Gap Transition of Monolayer InSe. *Phys. Chem. Chem. Phys.* **2017**, *19*, 21722−21728.

(49) Withers, F.; Del Pozo-Zamudio, O.; Mishchenko, A.; Rooney, A. P.; Gholinia, A.; Watanabe, K.; Taniguchi, T.; Haigh, S. J.; Geim, A. K.; Tartakovskii, A. I.; Novoselov, K. S. Light-Emitting Diodes by Band-Structure Engineering in van der Waals Heterostructures. *Nat. Mater.* **2015**, *14*, 301−306.

(50) Rivera, P.; Schaibley, J. R.; Jones, A. M.; Ross, J. S.; Wu, S.; Aivazian, G.; Klement, P.; Seyler, K.; Clark, G.; Ghimire, N. J.; Yan, J.; Mandrus, D. G.; Yao, W.; Xu, X. Observation of Long-Lived Interlayer Excitons in Monolayer MoSe$_2$-WSe$_2$ Heterostructures. *Nat. Commun.* **2015**, *6*, 6242.

(51) Peng, L.; Xian, J.-J.; Tang, P.; Rubio, A.; Zhang, S.-C.; Zhang, W.; Fu, Y.-S. Visualizing Topological Edge States of Single and Double Bilayer Bi Supported on Multilayer Bi(111) Films. *Phys. Rev. B: Condens. Matter Mater. Phys.* **2018**, *98*, 245108.

(52) Xia, H.; Li, Y.; Cai, M.; Qin, L.; Zou, N.; Peng, L.; Duan, W.; Xu, Y.; Zhang, W.; Fu, Y.-S. Dimensional Crossover and Topological Phase Transition in Dirac Semimetal Na$_3$Bi Films. *ACS Nano* **2019**, *13*, 9647−9654.

(53) Blöchl, P. E. Projector Augmented-Wave Method. *Phys. Rev. B: Condens. Matter Mater. Phys.* **1994**, *50*, 17953.

(54) Kresse, G.; Furthmüller, J. Efficiency of *ab-Initio* Total Energy Calculations for Metals and Semiconductors Using a Plane-Wave Basis Set. *Comput. Mater. Sci.* **1996**, *6*, 15.

(55) Kresse, G.; Joubert, D. From Ultrasoft Pseudopotentials to the Projector Augmented-Wave Method. *Phys. Rev. B: Condens. Matter Mater. Phys.* **1999**, *59*, 1758.

(56) Zhou, W.; Yu, G.; Rudenko, A. N.; Yuan, S. Tunable Half-Metallicity and Edge Magnetism of H-Saturated InSe Nanoribbons. *Phys. Rev. Mater.* **2018**, *2*, 114001.